Article

Phenyl-C61-Butyric Acid Methyl Ester Hybrid Solution for Efficient CH₃NH₃PbI₃ Perovskite Solar Cells

MiJoung Kim [1], MoonHoe Kim [1], JungSeock Oh [1], NamHee Kwon [1], Yoonmook Kang [2],* and JungYup Yang [1],*

[1] Department of Physics, Kunsan National University, Gunsan 54150, Korea
[2] KU-KIST Green School, Graduate School of Energy and Environment, Korea University, Seoul 02841, Korea
* Correspondence: ddang@korea.ac.kr (Y.K.); jungyup.yang@kunsan.ac.kr (J.Y.)

check for updates

Abstract: Organic–inorganic halide perovskite solar cells (PSCs) have excellent chemical, electronic, and optical properties, making them attractive next-generation thin-film solar cells. Typical PSCs were fabricated with a perovskite absorber layer between the TiO_2 electron-transport layer (ETL) and the 2,2′,7,7′-tetrakis-(N,N-di-4-methoxyphenylamino)-9,9′-spirobifluorene (Spiro-OMeTAD) hole-transport layer (HTL). We examined the influence of phenyl-C61-butyric acid methyl ester (PCBM) on the PSC device. PSCs using the PCBM layer as an ETL were investigated, and the absorber layer was coated by dissolving PCBM in a methyl ammonium lead iodide ($MAPbI_3$) precursor solution to examine the changes at the perovskite interface and inside the perovskite absorber layer. The PSCs fabricated by adding a small amount of PCBM to the $MAPbI_3$ solution exhibited a significantly higher maximum efficiency of 16.55% than conventional PSCs (14.34%). Fabricating the PCBM ETL and PCBM-$MAPbI_3$ hybrid solid is expected to be an efficient route for improving the photovoltaic performance.

Keywords: Perovskite photovoltaic devices; phenyl-C61-butyric acid methyl ester; $MAPbI_3$; Efficiency

1. Introduction

As energy consumption increases throughout the world, solar cells are expected to be a key technology for solving the energy problem, and organic–inorganic hybrid metal halides are emerging as a new class of absorber materials for solar-cell devices. Organic–inorganic halide perovskite solar cells (PSCs) are important candidates for thin-film solar cells owing to their low cost and high performance. Additionally, PSCs are widely considered as promising and next-generation photovoltaic devices [1–3]. The main advantages of PSCs are their low production cost and high efficiency. Another advantage of PSCs is that they are based on flexible, lightweight, and semi-transparent thin films [4–9]. PSCs have a light-absorber layer with an organic–inorganic hybrid perovskite crystal structure—typically methyl-ammonium lead tri-iodide ($CH_3NH_3PbI_3$, $MAPbI_3$)—fabricated on a transparent conductive oxide coated substrate. In a typical PSC, the device structure consists of a perovskite absorber layer that converts photons into electron/hole pairs in a photoactive layer, between the electron-transport layer (ETL) as transport photo-generated electrons and the hole-transport layer (HTL) as transport holes. N-type and p-type semiconductor materials have also been used for the ETL and HTL because they efficiently extract the photoexcited electrons and holes from the perovskite, respectively, which are transported to and then collected by a transparent, conducting oxide-coated glass substrate. Most high-efficiency PSCs include TiO_2 as an ETL and 2,2′,7,7′-tetrakis-(N,N-di-4-methoxyphenylamino)-9,9′-spirobifluorene (Spiro-OMeTAD)

as an HTL. However, TiO_2 and Spiro-OMeTAD materials exhibit poor stability under ultraviolet (UV) light irradiation and with unfavorable moisture and temperature conditions, respectively. Therefore, alternate materials have recently been intensively studied for enhancing the stability of PSCs. Among them, phenyl-C61-butyric acid methyl ester (PCBM) has been widely used for PSCs owing to its simple coating, small hysteresis effect, and high device performance as an ETL layer [10–13]. Recently, Huang et al. reported the PCBM passivation effect, where the C61 fullerene diffuses into the perovskite layer through the grain boundaries and further passivates the shallow trap state [14].

In the present study, we investigated the performance change of a PSC device when PCBM was mixed in the light absorber layer. PSCs with a PCBM layer as an ETL were also studied, and the absorber layer was coated by dissolving PCBM in a perovskite precursor solution (PCBM-MAPbI$_3$ hybrid solution) to investigate the changes at the perovskite interface and inside the perovskite absorber layer. According to the amount of PCBM in the MAPbI$_3$ precursor solution, the microstructures of the perovskite absorber layer were investigated. A low content of PCBM in the MAPbI$_3$ precursor solution yielded efficient electron transport, improving the charge-carrier extraction and transport. Therefore, a higher device efficiency (16.55%) was achieved compared to that of the conventional device (14.34%, without PCBM). This study provides a simple and practical route for improving photovoltaic performance.

2. Materials and Methods

2.1. Materials

To prepare the perovskite precursor, commercial material powders were used such as methylammonium iodide (MAI; 99%) and lead (II) iodide (PbI$_2$; 99.9985%). N,N-dimethylformamide (DMF; 99.8%) was used as the main solvent. To prepare the PCBM precursor solution, chlorobenzene (CB; 99.8%) and PCBM (99.9%) were used. To prepare the TiO$_2$ solution, 0.15 M titanium diisopropoxide dis(acetylacetonate) (75 wt% in isopropanol) was mixed in 1-butanol (99.8%). The Spiro-OMeTAD solution consisted of 72.3 mg Spiro-OMeTAD, 28.8 μl of 4-tert-butyl pyridine, and 17.5 μl of lithium bis(trifluoromethanesulfonyl)imide (Li-TFSI) solution in 1 ml CB. All chemicals were used as received, without any further purification.

2.2. Film Formation and Device Fabrication Procedure of n-i-p Perovskite Solar Cells (PSCs)

The fabrication process is described as follows. The patterned fluorine-doped tin oxide (FTO) coated glass substrates were washed with an alkaline detergent. Then, the FTO glass substrates were sequentially ultrasonically cleaned with acetone (15 min), ethyl alcohol (15 min), and isopropyl alcohol (15 min) and rinsed with deionized water. After the glass substrate was dried by a N$_2$ flow, UV-ozone (UVO) treatment was applied for 20 min to remove any organic residue. A TiO$_2$ solution as ETL was spin-coated onto the FTO substrate at 700 rpm for 8 s, 1000 rpm for 10 s, and 2000 rpm for 40 s, and then the substrates were annealed at 125 °C for 5 min in atmospheric air. This procedure was repeated three times to form an TiO$_2$ ETL with the appropriate thickness (about 128 nm). The TiO$_2$ was heated at 450 °C for 1 h to obtain an anatase crystal structure having a favorable crystal structure of the ETL layer, and then UVO treatment was applied again for 20 min. The MAPbI$_3$ was spin-coated via a one-step process in a dry N$_2$ ambient glovebox. The MAPbI$_3$ solution, which contained 461 mg of PbI$_2$, 159 mg of MAI, and 78 mg of dimethyl sulfoxide (DMSO) (molar ratio 1:1:1), was mixed in 600 mg of a DMF solution. Additionally, PCBM solutions were prepared by adding 20 mg of PCBM to 1 mL of CB. The PCBM solutions were directly mixed into the MAPbI$_3$ solution. The PCBM-MAPbI$_3$ hybrid solution was stirred at 70 °C for 1 h before spin-coating, and the volume ratios of MAPbI$_3$:PCBM were 1:1, 1:0.5, 1:0.1, 1:0.05, 1:0.01, and 1:0.005. The PCBM-MAPbI$_3$ hybrid solution with the 1:1 volume ratio was not well mixed; thus, the mixture was stirred overnight at 70 °C and then spin-coated. The PCBM-MAPbI$_3$ solutions were spin-coated at 4000 rpm for 25 s as the absorber layer of the solar cells, followed by annealing at 65 °C for 1 min and at 100 °C for 2 min to remove residual solvents.

Next, Spiro-OMeTAD solution was coated onto the perovskite absorber layer at 3000 rpm for 30 s. Finally, device fabrication was completed via the deposition of Au electrodes using a sputtering system. The detailed experimental methods for the device fabrication are presented in other papers [15,16].

The device structure is shown in Figure 1. Only MAPbI$_3$ (the most common perovskite light-absorber material) and MAPbI$_3$+PCBM mixed film were used as the solar cell absorber layer. The TiO$_2$ and Spiro-OMeTAD were used for the ETL and HTL, respectively. All the experimental perovskite photovoltaic devices had a normal (n-i-p) planar heterojunction structure.
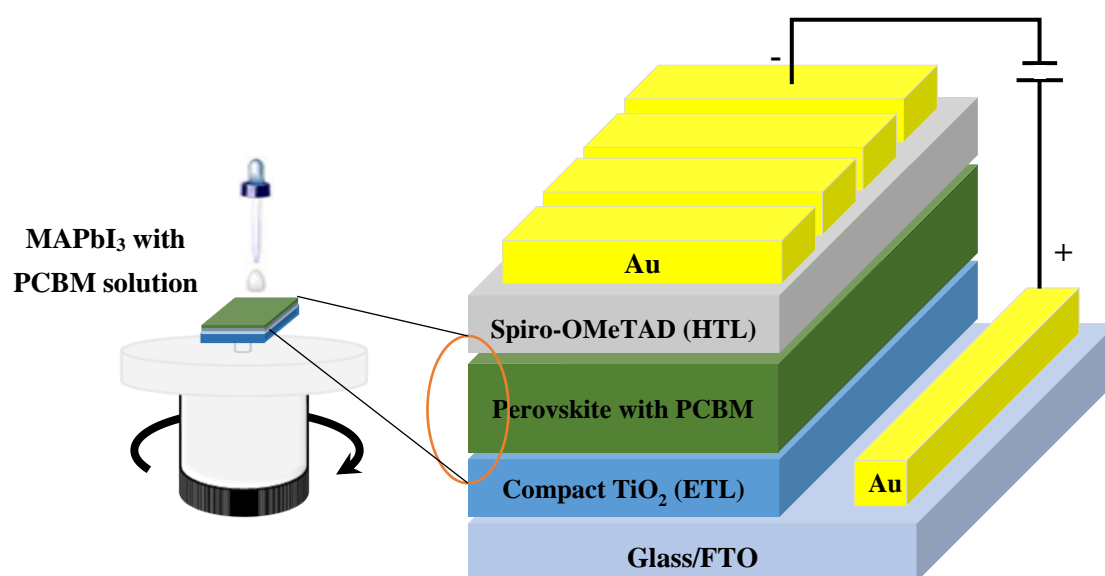

Figure 1. Schematic of the n-i-p normal device architecture of this study. MAPbI$_3$, methyl ammonium lead iodide; PCBM, phenyl-C61-butyric acid methyl ester; ETL, electron transport layer; HTL, hole transport layer; and FTO, fluorine-doped tin oxide.

2.3. Characterizations

The structural properties of the perovskite films were measured and analyzed via high-resolution X-ray diffraction (HR-XRD). The thermal properties of the PCBM-MAPbI$_3$ hybrid solution were verified using thermogravimetry and differential thermal analysis (TG-DTA). The chemical properties of PCBM-MAPBI$_3$ hybrid film were measured by Fourier-transform infrared spectroscopy (FTIR). Additionally, energy-dispersive X-ray spectroscopy (EDS) mapping was performed to elucidate the PCBM's location. To evaluate the quality of the absorber layer, we measured the photoluminescence (PL) and time-resolved PL (TRPL) of the MAPbI$_3$ films and PCBM-MAPbI$_3$ hybrid films with various PCBM contents (volume ratio from 0.5% to 100%). Current density–voltage (J–V) characterization of the PSCs was performed using a Keithley 2400 source meter under AM 1.5G 1-sun illumination. The illumination was calibrated using standard Si solar cells and a photometer.

3. Results and Discussion

3.1. Crystal Structure and FTIR Spectra of Phenyl-C61-Butyric Acid Methyl Ester– Methyl Ammonium Lead Iodide (PCBM-MAPbI$_3$) Hybrid Film

The HR-XRD data revealing the structural characteristics of the PCBM-MAPbI$_3$ films with (made from 0.1:1 solution) and without PCBM are shown in Figure 2. The diffraction pattern of MAPbI$_3$ exhibited peaks at 2θ = 13.97°, 28.15°, 40.63°, and 42.78°, corresponding to the (002), (004), (006), and (400) planes of the tetragonal crystal structure of perovskite, respectively [17,18]. As shown in Figure 2, the lattice diffraction peaks of the thin film based on the blend of MAPbI$_3$ and PCBM were consistent with those of the pristine MAPbI$_3$ film without PCBM. This indicates that the added fullerenes

did not destroy the MAPbI$_3$ crystal structures and had little effect on the MAPbI$_3$ crystal structure. Supplementary Table S1 presents the grain size of the crystallites for the principal diffraction peak, which was calculated using the Scherrer equation [19]. The perovskite grain size of the PCBM-MAPbI$_3$ hybrid film was comparable to that of the control MAPbI$_3$ film without PCBM.

Figure 3 present FTIR spectra of the MAPbI$_3$ film with and without PCBM. As shown in Figure 3, the FTIR spectra showed an observation of the stretching C = O vibration at 1750 cm^{-1} for the PCBM-MAPbI$_3$ hybrid film. However, the stretching C = O vibrations of the control MAPbI$_3$ film without PCBM could not observed. Therefore, elimination of their vibrations in FTIR spectra happened through complexation in the interface of C = O moiety with Pb atoms from perovskite, which is expected to reduce the charge recombination and increase the electron extraction in the MAPbI$_3$-PCBM hybrid film [20].
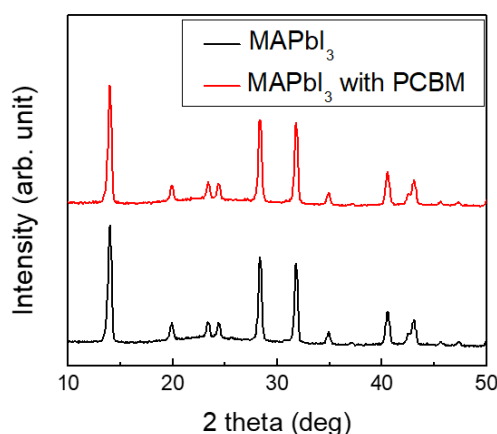

Figure 2. XRD patterns of films prepared from MAPbI$_3$ and MAPbI$_3$ mixed with PCBM (0.1:1 mixture ratio: 100 μL of PCBM mixed with 1000 μL of MAPbI$_3$ solution).
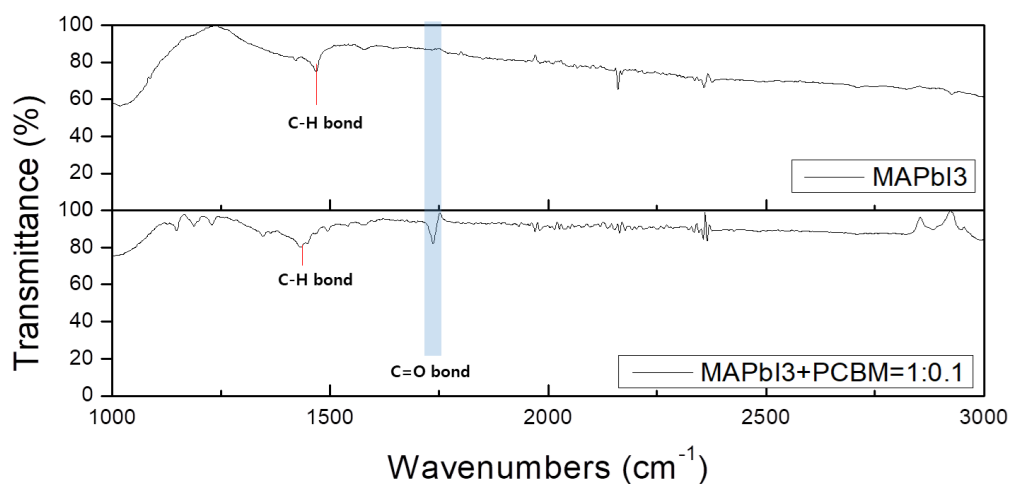

Figure 3. FTIR spectra for MAPbI$_3$ and PCBM-MAPbI$_3$ hybrid films.

3.2. Thermal Behavior of MAPbI$_3$, PCBM, and MAPbI$_3$ with PCBM

The thermal properties of the PCBM solution, MAPbI$_3$ precursor solution, and PCBM-MAPbI$_3$ mixture solution were investigated via simultaneous TG-DTA measurements in a N$_2$ atmosphere. From start to end, the weight-loss steps were delimited using the slope changes caused by thermal events in the DTA trace, which was recorded during the TG measurements. Figure 4a–c show the TG-DTA trace peaks recorded during the thermal degradation of PCBM, MAPbI$_3$, and PCBM-MAPbI$_3$, respectively. The inset in Figure 4a is enlarged data of the TG-DTA curve of PCBM in order to well distinguish data. From the TG-DTA plot shown in Figure 4a, two weight-loss steps were observed.

The first and second steps were the CB solvent and PCBM, respectively. From these data, PCBM had thermal stability up to approximately 380 °C and then began to lose weight. In contrast, four weight-loss steps were observed in the case of the MAPbI$_3$ precursor solutions with and without PCBM, as shown in Figure 4b,c. The first and second steps were the DMF solvent and DMSO weight-loss steps, respectively. As indicated by Figure 4b,c, in the third step, at approximately 400 °C, a weight-loss difference of approximately 0.6% was observed between the MAPbI$_3$ precursor solutions with and without PCBM. In the final step, the MAPbI$_3$ mixed with the PCBM solution had approximately 10% of its initial weight. This 10% remaining weight was due to the PCBM; thus, the PCBM-MAPbI$_3$ (0.1:1 volume ratio) was well mixed.
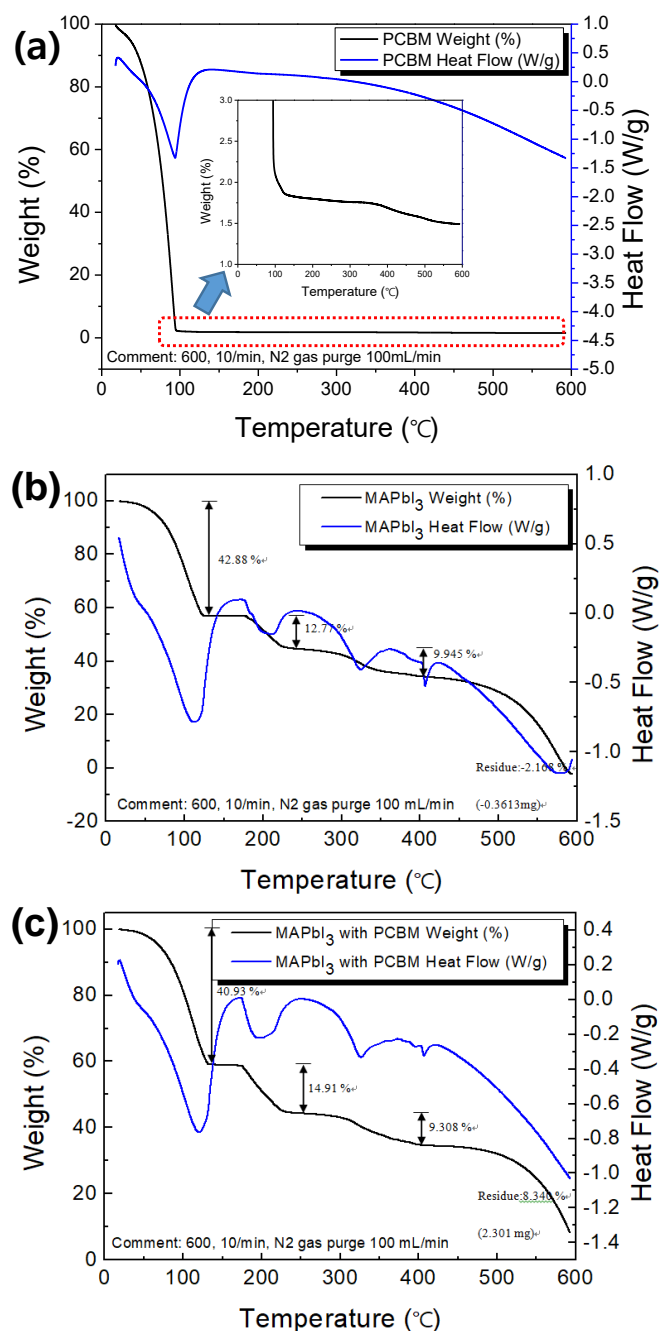

Figure 4. TG-DTA data for (**a**) PCBM, (**b**) MAPbI$_3$, and (**c**) the PCBM-MAPbI$_3$ hybrid solution in a N$_2$ atmosphere.

3.3. Photovoltaic Performance of Normal (n-i-p) Planar PSCs

Planar PSCs with a normal n-i-p structure (FTO/compact TiO_2/$MAPbI_3$ based absorber layer/Spiro-OMeTAD/Ag) were fabricated. The photovoltaic J–V characteristics of devices with different absorber layers are shown in Figure 5, and the corresponding device performance parameters are presented in Table 1. The different absorber layers were fabricated using $MAPbI_3$ with different PCBM mixture ratios (in volume percent). As shown in Figure 5a, the device performance (short-circuit current density, open circuit voltage, fill factor, and efficiency) was highest when the PCBM-$MAPbI_3$ mixture ratio was 0.005:1. When the PCBM mixture ratio was increased from 0.005:1 to 1:1, the device performance deteriorated. The best PSCs with a 0.005:1 mixture ratio exhibited improved device performance, with a short-circuit current density (J_{sc}) of 22.76 mA/cm^2, an open-circuit voltage (V_{oc}) of 1.0089 V, a fill factor (FF) of 72.2%, and an efficiency of 16.55%. This efficiency was significantly higher than that of 14.34% for pure $MAPbI_3$ (0:1). Additionally, the device with the 0.005:1 PCBM-$MAPbI_3$ mixed absorber layer had higher device performance than that with PCBM as the ETL layer (PCBM/$MAPbI_3$/Spiro-OMeTAD structure), as shown in Supplementary Figure S2. Thus, introduction of PCBM into the $MAPbI_3$ perovskite precursor enhanced the photovoltaic performance of the PSCs. We attributed the increased J_{sc} in the presence of a small amount of PCBM to the improved electron transport, and we attributed the increased FF to the improved film quality. Therefore, it was considered that when the fullerene derivative PCBM was blended into the perovskite precursor, the PCBM dispersed into the perovskite precursor passivated defects during perovskite self-assembly, improving the quality of the photoactive layer by filling pinholes and vacancies between perovskite grains [17]. To verify the impact of the PCBM on the perovskite materials, PCBM with different concentrations were blended into the precursor solution. At PCBM concentrations higher than 0.005:1, the solar-cell performance was degraded, and the number of dissolved fullerenes affected the overall performance of the PSCs. Experimentally, we can conclude that perovskite coating with the PCBM-$MAPbI_3$ hybrid solution is essential for obtaining perovskite absorbers with characteristics suitable for planar-type solution-processed PSCs. The proposed method is very simple with regard to the precursor preparation and processing steps, and adding a small amount of PCBM to the perovskite solution can improve the device efficiency by 16.55%. It can be widely used for low-temperature and solution-processed planar PSC technology.

Table 1. Device current-voltage characteristics at various PCBM ratios.

Structure	$MAPbI_3$:PCBM Ratio (volume %)	J_{sc} (mA/cm^2)	V_{oc} (V)	FF (%)	Efficiency (%)
FTO/TiO_2/PCBM-$MAPbI_3$/ Spiro-OMeTAD/Au	1:1	13.79	0.8150	59.85	6.73
	1:0.5	16.01	0.8591	54.07	7.43
	1:0.1	17.37	1.006	61.7	11.43
	1:0.05	17.87	1.012	66.1	11.95
	1:0.01	22.74	1.0032	61.5	14.04
	1:0.005	22.76	1.0089	72.2	16.55
FTO/TiO_2/$MAPbI_3$/Spiro-OMeTAD/Au	1:0 (Ref)	21.82	0.9683	67.9	14.34

(**a**)

(**b**)

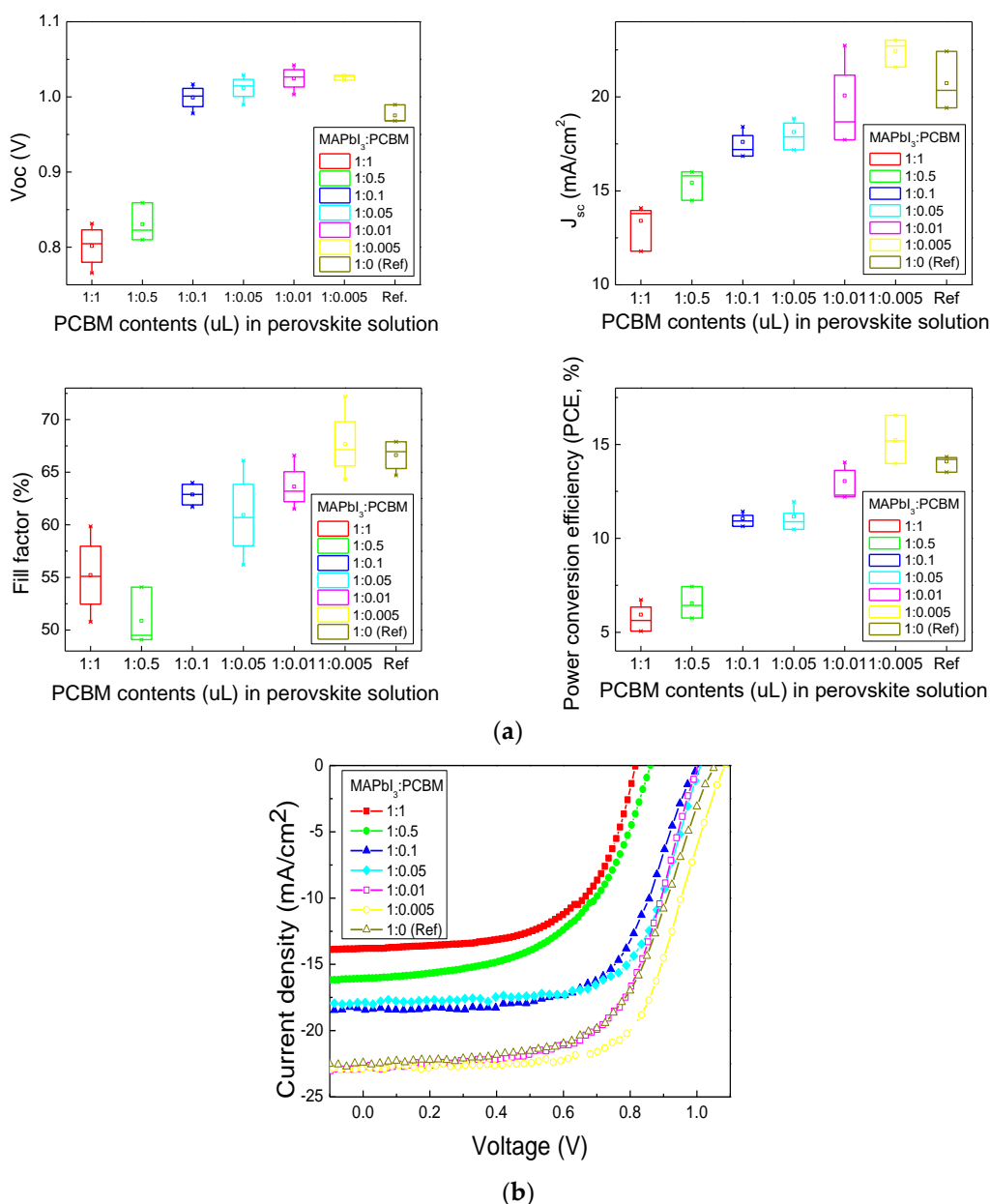**Figure 5.** (**a**) Photovoltaic properties of MAPbI₃ perovskite solar cells (V_{oc}, J_{sc}, FF, and efficiency) prepared with MAPbI₃ only and with different PCBM-MAPbI₃ mixture ratios; (**b**) J–V characteristics of the MAPbI₃ PSCs prepared with MAPbI₃ only and the PCBM-MAPbI₃ hybrid solutions of different mixture ratios.

3.4. Difference in C Content Between Grain Interior and Grain Boundaries

As mentioned above and in reference [17], improved device performance is attributed to the PCBM passivation at the grain boundaries of the MAPbI₃ film. To determine whether PCBM existed in grain boundaries of MAPbI₃, we measured the PCBM distribution in the MAPbI₃ films using scanning electron microscopy (SEM)-EDS mapping, as shown in Figure 6. The cross-sectional SEM images in Figure 6a,b show the microstructure of the MAPbI₃ films with and without PCBM on the TiO₂ ETL, respectively. The insets in Figure 6a,b present the EDS spectra for each point (3: grain interior; 4: grain boundary) shown in the SEM photograph. We attempted to determine the weight percent (wt%) of C using EDS mapping because it is difficult to measure the PCBM directly. The PCBM is a C-based fullerene derivative material ($C_{72}H_{14}O_2$) comprising organic components. We observed

a difference between the intra-grain and grain boundary C contents, as shown in Table 2. For the perovskite fabricated with the PCBM-MAPbI$_3$ (0.005:1) hybrid solution, there was a large difference in the C content (+2.54 wt%) between the grain interior and grain boundary. For the perovskite fabricated with only the MAPbI$_3$ solution, the difference (–3.22 wt%) was smaller. The C content of the PCBM-MAPbI$_3$ (0.005:1) film was higher than that of the MAPbI$_3$ film (for both the grain interior and the grain boundary). The experimental results confirm that PCBM was suggested to be preferentially located at the perovskite grain boundaries [17,21].
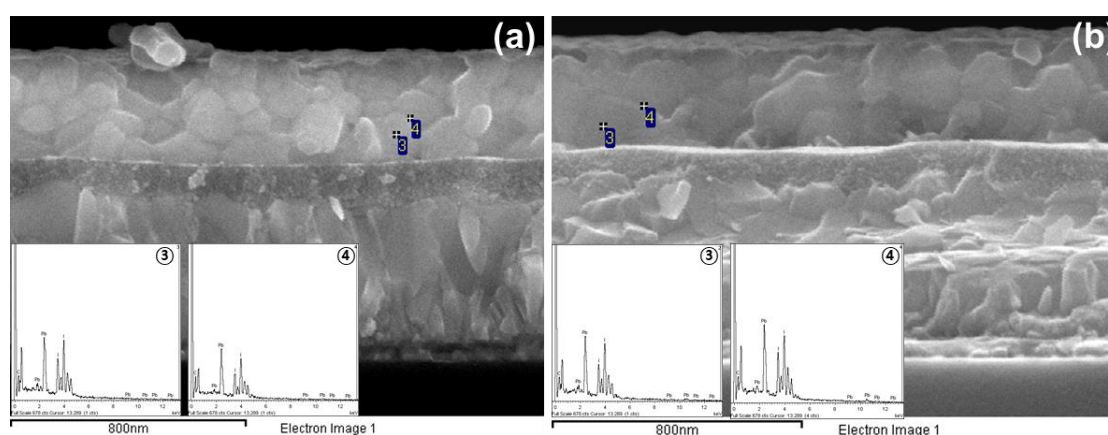

Figure 6. Cross-sectional SEM images showing the microstructure of the MAPbI$_3$ films (**a**) with and (**b**) without PCBM on the TiO$_2$ ETL. The insets in (**a**,**b**) present EDS spectra for each point (3: grain interior; 4: grain boundary).

Table 2. Elemental composition measured using EDS.

Samples	MAPBI$_3$:PCBM = 1:0.005			Only MAPbI$_3$		
Element	Intra-Grain (wt%)	Grain Boundary (wt%)	Difference	Intra-Grain (wt%)	Grain Boundary (wt%)	Difference
C K	21.29	23.83	+2.54	20.75	17.53	–3.22
I L	48.48	44.69	+3.79	48.72	50.61	+1.89
Pb M	30.23	31.48	+1.25	30.53	31.87	+1.34
Totals	100.00	100.00		100.00	100.00	

3.5. Steady-State and TRPL Decay

In order to further investigate the origin of the enhanced photovoltaic performance of PSCs using the PCBM-MAPbI$_3$ hybrid film, we performed steady-state PL and TRPL measurements for elucidating the charge-extraction phenomena of the added PCBM in the mixed perovskite layers and the charge-transfer kinetics between the MAPbI$_3$ films and the transport layers, respectively. Figure 7a shows the steady-state PL spectra of only MAPbI$_3$ and PCBM-MAPBI$_3$ hybrid films on glass substrates. As shown in Figure 7a, a significant PL quenching effect was observed when the perovskite layer formed with PCBM, indicating an efficient charge-transfer process at the perovskite layer [17,22]. In addition, the PL intensity of the perovskite was significantly reduced depending on the PCBM-MAPbI$_3$ mixing ratio, which implies the difference charge transfer of MAPbI$_3$ film depending on the PCBM ratio. As mentioned above from EDS results, it can be assumed that the added PCBM is filled with grain boundaries in the MAPbI$_3$ film, producing continuous pathways for electron extraction. Figure 7b shows TRPL data measured by monitoring the peak emission at 767 nm. The corresponding lifetime of the TRPL decay curve fitted to a quadratic-exponential function [23] is presented in Table 3. Fitting the data with a bi-exponential decay function yielded two carrier lifetimes, indicating that the PL decay of perovskite occurred through two relaxation pathways: fast and slow decay processes. The fast and slow decays were attributed to PL quenching in the perovskite

films through charge-carrier transfer at the interface and radiative decay, respectively [11]. For the MAPbI$_3$ perovskite film without PCBM, a PL lifetime as long as 14.64 ns was observed. This long lifetime is essential for large exciton/carrier diffusion lengths to allow large film thicknesses for light harvesting [14]. When PCBM-MAPbI$_3$ was mixed, rapid decay of lifetime was observed. The fast decay for the lifetime, which indicates that most of the electrons were efficiently delivered to the PCBM, suggests that the PCBM-MAPbI$_3$ mixed layer induced rapid carrier extraction. The lifetime depending on the mixture ratio of PCBM indicated increased fullerene–MAPbI$_3$ interfaces and facilitated more efficient electron extraction from the perovskite, which contributed to stronger fluorescence quenching and accelerated PL decay. Therefore, by dissolving the added PCBM in the MAPbI$_3$ solution, both the electron-extraction and electron-transport abilities were significantly enhanced, leading to a far shorter lifetime. Thus, the formed layers had charge-extraction properties, which are beneficial for photovoltaic applications. Additionally, the results suggest that the incorporation of PCBM in MAPbI$_3$ can improve the charge-carrier transfer efficiency at grain boundaries, which can suppress the charge-carrier recombination and increase the performance of the photovoltaic device.
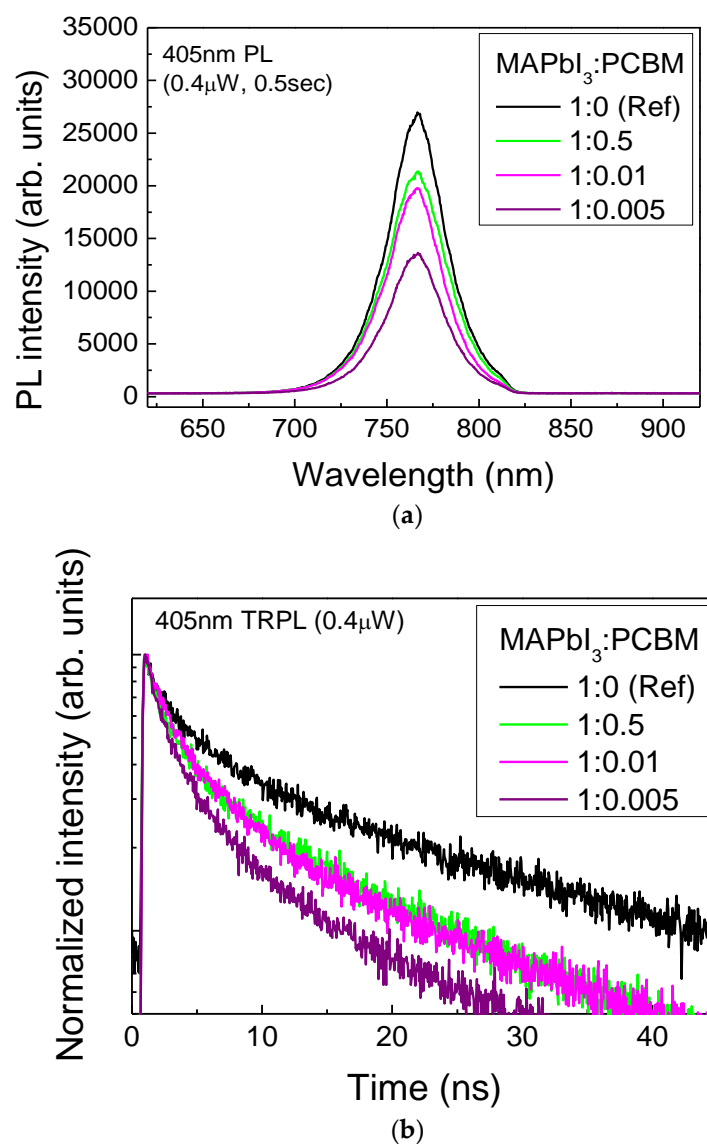

(a)

(b)

Figure 7. (**a**) Steady-state photoluminescence (PL) of films prepared from MAPbI$_3$ and MAPbI$_3$ mixed with PCBM; (**b**) time-resolved photoluminescence (TRPL) spectra of corresponding films prepared from MAPbI$_3$ and MAPbI$_3$ mixed with PCBM.

Table 3. Comparison of the lifetimes at various PCBM ratios.

	1:0.5	1:0.01	1:0.005	1:0 (Ref)
A1	0.44276	0.41395	0.37235	0.70634
t1	13.18063	12.4614	10.11754	1.96384
A2	0.94474	0.93156	1.1608	0.48923
t2	1.67703	2.06318	1.62432	16.78579
τ	10.72439151	9.63879019	7.284585908	14.64394564

4. Conclusions

PCBM-MAPbI$_3$ hybrid solutions with various concentrations of PCBM were prepared. This PCBM-MAPbI$_3$ hybrid mixing technique offered recombination inhibition because of the reduction of vacancies in the grain interior and the recombination center at the grain boundaries for spin-coated MAPbI$_3$ films. TiO$_2$-based planar PSCs fabricated using the PCBM-MAPbI$_3$ hybrid solution exhibited an enhanced efficiency. The PCBM content was low, and the PCBM was able to passivate defects at the grain boundaries of MAPbI$_3$. A champion efficiency of 16.55% was obtained in PSCs of the n-i-p normal planar device prepared using PCBM-MAPbI$_3$ with a 0.005:1 mixture ratio. The proposed hybrid mixing technique with a PCBM additive can facilitate the fabrication of planar perovskite devices with enhanced PV performances.

Supplementary Materials: The following are available online at http://www.mdpi.com/2071-1050/11/14/3867/s1, Figure S1: Figure S1. Photograph of the MAPbI$_3$ precursor solution. The mixed materials made using solutions with various PCBM additive concentrations (5, 10, 50, 100, 500, and 1000 μL) and a 1000-μL MAPbI$_3$ solution are presented in this figure. As shown in this figure, the pristine PCBM-MAPbI$_3$ precursor (0:1) solution exhibited a bright yellow color, and its color changed to dark brown with an increase in the PCBM concentration from 0.005 to 1. Figure S2. J–V characteristics of the FTO/PCBM/MAPbI$_3$/Spiro-OMeTAD/Au solar cells. Table S1. Grain sizes (unit: Å) of the perovskite films.

Author Contributions: Conceptualization, M.K. (MiJoung Kim) and J.Y.; formal analysis, M.K. (MoonHoe Kim), J.O., and N.K.; project administration, J.Y., Y.K.; writing—original draft, M.K. (MiJoung Kim).

Conflicts of Interest: The authors declare no conflict of interest.

References

1. Tonui, P.; Oseni, S.O.; Sharm, G.; Yan, Q.; Mola, G.T. Perovskites photovoltaic solar cells: An overview of current status. *Renew. Sust. Energ. Rev.* **2018**, *91*, 1025–1044. [CrossRef]
2. Fang, F.; Chen, J.; Wu, G.; Chen, H. Highly efficient perovskite solar cells fabricated by simplified one-step deposition method with non-halogenated anti-solvents. *Org. Electron.* **2018**, *59*, 330–336. [CrossRef]
3. Cao, W.; Xue, J. Recent progress in organic photovoltaics: Device architecture and optical design. *Energy Environ. Sci.* **2014**, *7*, 2123–2144. [CrossRef]
4. Noh, J.H.; Im, S.H.; Heo, J.H.; Mandal, T.N.; Seok, S.I. Chemical management for colorful, efficient, and stable inorganic-organic hybrid nanostructured solar cells. *Nano Lett.* **2013**, *13*, 1764–1769. [CrossRef] [PubMed]
5. D'Innocenzo, V.; Grancini, G.; Alcocer, M.J.; Kandada, A.R.; Stranks, S.D.; Lee, M.M.; Lanzani, G.; Snaith, H.J.; Petrozza, A. Excitons versus free charges in organo-lead trihalide perovskites. *Nat. Commun.* **2014**, *5*, 3586. [CrossRef]
6. Wehrenfennig, C.; Eperon, G.E.; Johnston, M.B.; Snaith, H.J.; Herz, L.M. High charge carrier mobilities and lifetimes in organolead trihalide perovskites. *Adv. Mater.* **2014**, *26*, 1584–1589. [CrossRef] [PubMed]
7. Lv, Y.; Si, D.; Song, X.; Wang, K.; Wang, S.; Zhao, Z.; Hao, C.; Wei, L.; Shi, Y. Pseudo halogen-based 2D perovskite: A more complex thermal degradation mechanism than 3D perovskite. *Inorg. Chem.* **2018**, *57*, 2045–2050. [CrossRef]

8. Liu, D.B.; Wang, G.; Wu, F.; Wu, R.; Chen, T.; Ding, B.F.; Song, Q.L. Crystallization process of perovskite modified by adding lead acetate in precursor solution for better morphology and higher device efficiency. *Org. Electron.* **2017**, *43*, 189–195. [CrossRef]

9. Zeng, X.; Zhou, T.; Leng, C.; Zang, Z.; Wang, M.; Hu, W.; Tang, X.; Lu, S.; Fang, L.; Zhou, M. Performance improvement of perovskite solar cells by employing a CdSe quantum dot/PCBM composite as an electron transport layer. *J. Mater. Chem. A* **2017**, *5*, 17499–17505. [CrossRef]

10. Li, F.; Ma, C.; Wang, H.; Hu, W.; Yu, W.; Sheikh, A.D.; Wu, T. Ambipolar solution-processed hybrid perovskite phototransistors. *Nat. Commun.* **2015**, *6*, 8238. [CrossRef]

11. Wu, Y.; Yang, X.; Chen, W.; Yue, Y.; Cai, M.; Xie, F.; Bi, E.; Islam, A.; Han, L. Perovskite solar cells with 18.21% efficiency and area over $1\,cm^2$ fabricated by heterojunction engineering. *Nat. Energy* **2016**, *1*, 16148. [CrossRef]

12. Rafael, S.T.; Jorge, P.; Inés, G.B.; Silvia, C.; Ivet, K.; Ramón, T.Z.; Nazario, M.; Juan, L.D. Modified fullerenes for efficient electron transport layer-free perovskite/fullerene blend-based solar cells. *ChemSusChem* **2017**, *10*, 2023–2029.

13. Silvia, C.; Michael, S.; Wolfgang, R.T.; Philippe, J.H.; Sebastian, F.W.; Konrad, D.; Silver, H.T.-C.; Amita, U.; Shaik, M.Z.; Anders, H.; et al. Poly(ethylene glycol)–[60]Fullerene-based materials for perovskite solar cells with improved moisture resistance and reduced hysteresis. *ChemSusChem* **2018**, *11*, 1032–1039.

14. Shao, Y.; Xiao, Z.; Bi, C.; Yuan, Y.; Huang, J. Origin and elimination of photocurrent hysteresis by fullerene passivation in $CH_3NH_3PbI_3$ planar heterojunction solar cells. *Nat. Commun.* **2014**, *5*, 5784. [CrossRef] [PubMed]

15. Ahn, N.Y.; Son, D.Y.; Jang, I.H.; Kang, S.M.; Choi, M.S.; Park, N.G. Highly reproducible perovskite solar cells with average efficiency of 18.3% and best efficiency of 19.7% fabricated via Lewis base adduct of lead(II) iodide. *JACS* **2015**, *137*, 8696–8699. [CrossRef]

16. Son, D.Y.; Lee, J.W.; Choi, Y.J.; Jang, I.H.; Lee, S.H.; Yoo, P.J.; Shin, H.J.; Ahn, N.Y.; Choi, M.S.; Kim, D.H.; et al. Self-formed grain boundary healing layer for highly efficient $CH_3NH_3PbI_3$ perovskite solar cells. *Nat. Energy* **2016**, *1*, 16081. [CrossRef]

17. Xu, J.; Buin, A.; Ip, A.H.; Li, W.; Voznyy, O.; Comin, R.; Yuan, M.; Jeon, S.; Ning, Z.; McDowell, J.J.; et al. Perovskite–fullerene hybrid materials suppress hysteresis in planar diodes. *Nat. Commun.* **2015**, *6*, 7081. [CrossRef]

18. Luo, S.; Daoud, W.A.; Luo. Crystal structure formation of $CH_3NH_3PbI_{3-x}Cl_x$ perovskite. *Materials* **2016**, *9*, 123. [CrossRef]

19. Cullity, B.D.; Stock, S.R. *Elements of X-Ray Diffraction*, 3rd ed.; Prentice-Hall Inc.: Upper Saddle River, NJ, USA, 2001; pp. 167–171. ISBN 0-201-61091-4.

20. Tian, C.; Castro, E.; Wang, T.; German, B.S.; Gloria, R.; Luis, E. Improved performance and stability of inverted planar perovskite solar cells using fulleropyrrolidine Layers. *ACS Appl. Mater. Interfaces* **2016**, *8*, 31426–31432. [CrossRef]

21. Jorge, P.; Juan, L.D.; Ramón, T.Z. Physicochemical phenomena and application in solar cells of perovskite:fullerene films. *J. Phys. Chem. Lett.* **2018**, *9*, 2893–2902.

22. Liu, X.; Huang, P.; Dong, Q.; Wang, Z.; Zhang, K.; Yu, H.; Lei, M.; Zhou, Y.; Song, B.; Li, Y. Enhancement of the efficiency and stability of planar p-i-n perovskite solar cells via incorporation of an amine-modified fullerene derivative as a cathode buffer layer. *Sci. China Chem.* **2016**, *60*, 136–143. [CrossRef]

23. Redinger, A.; Levcenko, S.; Hages, C.J.; Greiner, D.; Kaufmann, C.A.; Unold, T. Time resolved photoluminescence on $Cu(In, Ga)Se_2$ absorbers: Distinguishing degradation and trap states. *Appl. Phys. Lett.* **2017**, *110*, 122104. [CrossRef]